

Application of Multi-Static Inversion Algorithms to Landmine Detection

Ali Cafer Gürbüüz, Tegan Counts, Kangwook Kim,

James H. McClellan and Waymond R. Scott Jr. *

Georgia Institute of Technology
Atlanta, GA 30332-0250;

ABSTRACT

Multi-static ground-penetrating radar (GPR) uses an array of antennas to conduct a number of bistatic operations simultaneously. The multi-static GPR is used to obtain more information on the target of interest using angular diversity. An entirely computer controlled, multi-static GPR consisting of a linear array of six resistively-loaded vee dipoles (RVDs), a network analyzer, and a microwave switch matrix was developed to investigate the potential of multi-static inversion algorithms. The performance of a multi-static inversion algorithm is evaluated for targets buried in clean sand, targets buried under the ground covered by rocks, and targets held above the ground (in the air) using styrofoam supports. A synthetic-aperture, multi-static, time-domain GPR imaging algorithm is extended from conventional mono-static back-projection techniques and used to process the data. Good results are obtained for the clean surface and air targets; however, for targets buried under rocks, only the deeply buried targets could be accurately detected and located.

Keywords: Multistatic Imaging, Ground penetrating radar (GPR), landmine detection, prestack migration, backprojection, three layer model

1. INTRODUCTION

Ground Penetrating Radar (GPR) has been shown in certain circumstances to be an efficient subsurface imaging tool for landmine detection due to its capability of detecting both metal and non-metal objects using dielectric discontinuities.¹ Most GPRs are implemented using a bistatic configuration. Bistatic systems use two different antennas, one for transmitting and one for receiving, separated by a fixed distance. A multistatic system is a combination of several bistatic pairs at varying separations. The potential benefit of a multistatic system over mono- or bistatic systems is the opportunity to obtain more information on the target by taking advantage of the angular diversity from different T-R (transmitter-receiver) pairs. This type of information is believed to be valuable in the presence of high clutter; in land mine detection this includes rocks, soda cans, plant debris, soil inhomogeneities etc. A multistatic GPR has been developed and scanned over three sets of scenarios.²

1.1. Imaging Algorithm

Raw data is imaged using time-domain backprojection. Although it is more computationally intensive than frequency-domain backprojection, modeling wave refraction at known interfaces (such as air-ground) is more straightforward with this technique. Also, this algorithm can easily model the different T-R spacings in a direct manner. Details of the algorithm are considered in Section 2.

1.2. Experiment Setup

An entirely computer controlled, multi-static GPR consisting of a linear array of six resistively-loaded vee dipoles (RVDs), a network analyzer, and a microwave switch matrix was developed.³ A picture and a diagram of the system are shown in Fig. 1. Detailed information about resistive vee antennas has been published.²

This work is supported under MURI by the U.S. Army Research Office under contract number DAAD19-02-1-0252
Further author information: (Send correspondence to Ali Cafer Gürbüüz): E-mail: alicaffer@ece.gatech.edu

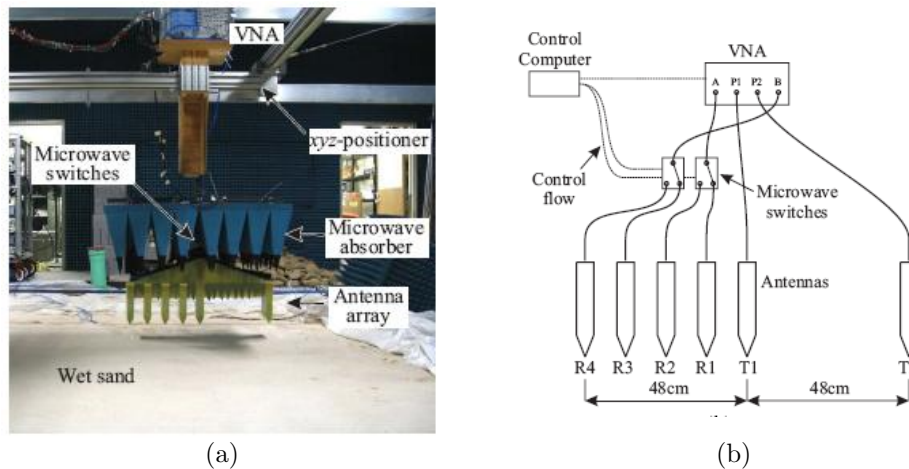


Figure 1. (a) Picture of multistatic GPR system, (b) System diagram.

The antenna array is scanned over several different scenarios. First, the antenna is raised and scanned over targets sitting on a foam platform (Fig. 2 (a)). This is done to simulate targets in freespace; it is useful for evaluating the antenna and imaging algorithms without the complexities of a multi-layered media. Targets scanned in this configuration include a 1" metal sphere and a plywood cutout in the shape of the letters GT. The second scenario is land mines buried in damp, compacted sand with a smooth surface. A variety of anti-tank and anti-personnel mines are used. The third scenario is a repeat of the buried land mines with a strongly cluttered surface. River rocks are placed on the surface of the sand (Fig. 2 (b)) to simulate clutter. A second cluttered experiment involves burying a plexiglass room.



Figure 2. (a) Air target scan configuration, (b) Surface cluttered with river rocks.

2. THEORY

2.1. Backprojection of a bistatic pair

As a GPR is scanned over a surface above a point-like target, the target response is a hyperboloid surface in the space-time domain. Typical time-domain backprojection algorithms implement coherent summations along the hyperboloid surface at each pixel in the image domain. The backprojection algorithm⁴ employed in this work is

$$f(x_T, y_T, z_T, m) = \frac{1}{2\pi} \int \int \frac{\cos\theta}{vr} \frac{\partial}{\partial t} P_{in}(x_{in}, y_{in}, t_d, m) dx dy \quad (1)$$

where $P_{in}(x_{in}, y_{in}, t_d)$ is the measured data at CMP antenna position (x_{in}, y_{in}) from T-R pair m at time t_d , and $\frac{\cos\theta}{vr} \frac{\partial}{\partial t}$ is the aperture weighting function. A CMP antenna position simply means the data taken while the particular T-R pair was centered around the point (x_{in}, y_{in}) ; the need for this convention arises due to the positioning of the antennas on the scan unit. In this work, the time differentiation in the weighting function is used for targets in the air but not for buried targets. The effect of differentiation is to emphasize high frequency content. While this is helpful for air targets which are illuminated by the entire frequency band of the antenna, it is not helpful for subsurface targets since high frequencies do not propagate into the ground. In the aperture weighting function, $\cos\theta$ is the obliquity factor, and it is given by the cosine of the angle between the direction of propagation and the vertical axis z . $1/vr$ is the spherical spreading factor where v is the wave velocity and the r is the distance between antenna position (x_{in}, y_{in}, z_{in}) and target position (x_T, y_T, z_T) . t_d is the round trip travel time of the transmitted signal from transmitter, to the target point, and back to the receiver. Calculation of t_d depends on the number of layers used to model the scan region. Finally, the integrals in Eq. 1 are evaluated as sums over a finite aperture to save processing time. The aperture will always be centered around the target point. This algorithm was implemented in Fortran 90 using MPI to run on parallel machines. The formation of images in a 3-D scenario takes approximately 2-3 minutes per pair.

2.2. Layer Modeling

An important part of subsurface imaging is the modeling of the refraction of the electromagnetic waves at the air ground boundary. In general when an electromagnetic wave encounters the boundary between two different media, the propagation direction changes according to Snell's law. The exact calculation of the refraction point requires the solution of a 4th degree polynomial. Instead, an approximate solution for the refraction point⁵ is given by

$$x_2 = x_3 + \sqrt{\frac{\epsilon_1}{\epsilon_2}}(x_1 - x_3) \quad (2)$$

where x_1 , x_2 , and x_3 are defined in Fig. 3 (a). For highly cluttered surfaces a 3-layer model is used. For this experiment, the layers represent air, clutter in the form of river rocks, and sand. Figure 3 (b) details the approximate path from the antenna position to the target position. At each boundary path is diffracted according to (2). The combination of these two boundary conditions results in

$$y_1 = y_0 + \frac{(y_T - y_0)v_2 L}{1 - \frac{z_0 v_3}{(z_0 - L)v_2} (1 - \frac{L}{z_T})} \quad y_2 = y_0 + z_0 \frac{(y_1 - y_0)v_3}{(z_0 - L)v_2}. \quad (3)$$

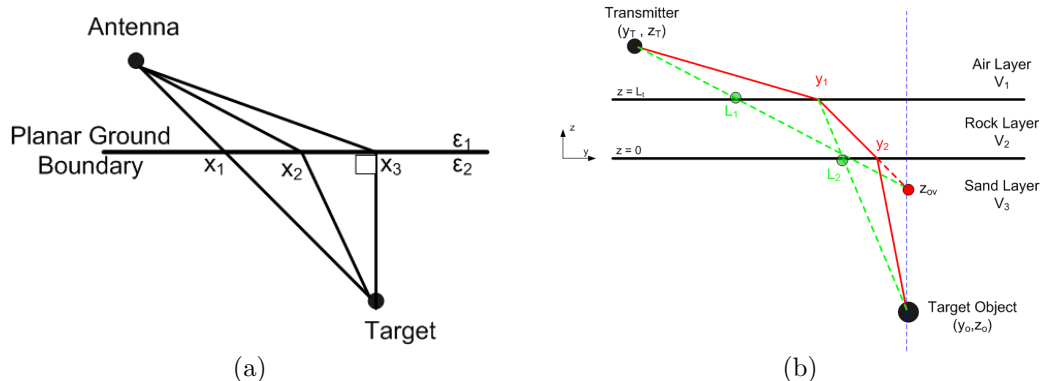


Figure 3. (a) Two layer model, (b) Three layer model.

2.3. Scan Region Limitations

One important problem in combining results from different TR pairs is which pairs to use. The antenna beamwidth limits the depths which a certain T-R pair can operate. Assuming each has a certain beamwidth, θ_i , within which they can send and receive power, a target must lie in the intersection of the antenna footprint regions as shown in Fig. 4 (a) for the two layer case. The limitation on the T-R distance, d_{TR} , required to receive a signal from a target at depth d is

$$d_{TR} < 2(h \tan \theta_i + d \tan \theta_r) \quad (4)$$

where θ_i is the incident angle and θ_r is the refraction angle. A constant wave velocity in the sand has been assumed for all cases. The refraction angle depends on the incident angle and the relative permittivities of the medium through Snell's law. The maximum T-R distance for the antenna configuration used in this experiment and empirically determined soil permittivity is given in Fig. 4 (b).

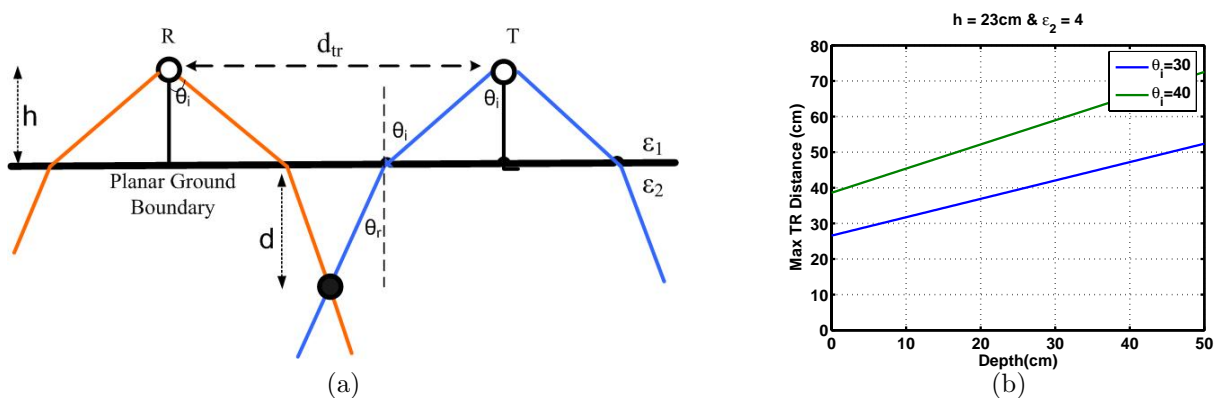


Figure 4. (a) Maximum T-R distance case, (b) Maximum T-R distance for varying depths for $h = 23\text{cm}$ and $\epsilon_2 = 4$

In the subsurface experiments, maximum target depths do not exceed 20 cm, and the antenna beamwidth, θ_i , is measured to be between 30 and 40 degrees. Pair combination T1-R3 has a separation of 36 cm, so it is definitely usable. Pair combination T1-R4 has a separation of 48 cm, and it will be used even though it is only barely in the antenna separation range.

2.4. Combination of bistatic pairs

Images are formed for the individual pairs by backprojection, and then they are coherently summed. The most critical aspects of obtaining a good sum image is the time/depth alignment of the individual images. In a physical GPR there are three interrelated parameters that are dominant in setting this alignment: wave speed in the target media, location of the phase center of the antenna, and time delay from the antenna terminal to the phase center. It is widely known that the backprojection algorithm strongly depends on velocity estimation. The complex nature of the phase center in resistive-vee dipole antennas is still under investigation, so to simplify the imaging analysis it was assumed to be a constant point. In this antenna system, the lengths of cables that connect the antennas to the analyzer are calibrated out by approximating the cable effects as phase shifts only. In theory, we would like to calibrate at the phase center of the antenna, but since this is physically impossible we calibrate at the coaxial connector at the end of the antenna package. The remaining phase shift, or time delay in the time domain, from that connector to the phase center affects the time reference of the antenna response. Since this time depends on the location of the phase center, an appropriate time delay was selected based on the chosen phase center. All targets in this paper have been imaged with a phase center of 13 cm above the tip of the antenna, a time delay from the connector to the phase center of 750 ps, an air velocity of 3.00×10^8 m/s, and a sand velocity of 1.50×10^8 m/s. The sand velocity was chosen to obtain the best alignment in a moveout graph.

3. RESULTS

3.1. Air Targets

A 1" metal sphere and a piece of plywood cut into the shape of the letters GT (38.5cm x 46.5cm x 1.8cm) are elevated 49.5 cm below the phase center and level with the ground on a styrofoam support. The reflections from the targets are measured using 4 T-R pairs, and each pair is backprojected using Eq. 1. A one layer model is used with a 120 cm x 120 cm synthetic aperture stepped at 2 cm.

Fig. 5 - 7 show the results of processing the sphere with this algorithm. Fig. 5 is a moveout of the migrated output of the four pairs; the vertical column of data from each pair that goes through the center of the sphere is plotted side-by-side. It shows a very good time alignment of the data; this provides confidence going forward that the chosen time alignment parameters (Section 2.4) are close to their actual values.

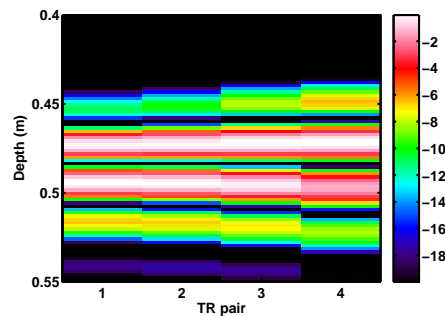


Figure 5. Moveout of 1" Sphere.

Fig. 6 shows slices of the migrated data for a narrow pair, a wide pair, and the coherent sum of the narrowest four pairs. The narrower pairs produce tighter images. Not surprisingly, the image in the $y = 0$ plane is stretched more than the $x = 0$ plane; this is due to the orientation of the resistive-vee antennas. Multistatic combination does not appear to be significantly better than the single pair scans. Fig. 7 presents another way of observing the data. These are -5 dB (relative to the maximum of each image) isofigures. Again, the multistatic combination does not appear to improve the image, but it is important that it does not deform the image either.

Migrated slices of the GT sign for pair T1-R1 and the multistatic combination of the narrowest four pair are shown in Fig. 8. The GT sign has a similar moveout alignment to the sphere. The migration algorithm is still performing well despite the more complex target, but multistatic combination is still not significantly helpful.

3.2. Buried Mines

In this configuration, multiple targets - such as antipersonnel and antitank mines, metal spheres, nylon cylinders and mine stimulants - are buried in a sandbox with an area of 180 cm x 180 cm. A picture of the buried targets is shown in Fig. 9(a). Figure 9(b) shows the burial locations, types and depths of the targets.

The datasets from different T-R pairs are migrated by (1) using a 2 layer model for the ground. Fig. 10 shows the moveout for two different targets, one shallow and one deep. The flat moveout indicates that the time alignment is good. Both shallow and deep targets are aligned well. Full migration results are shown in Figs. 11 and 12 for the narrowest pair and the coherent sum of the four narrowest pairs. The narrowest pair has the best result of any single pair. Multistatic combination looks promising in this case, but the horizontal layers in the multistatic image interfere with target recognition. It is not known whether this layering is an artifact of the algorithm, real layering in the sand, or artifacts from the air-ground interface. The isofigure in Fig. 12 indicates that pair T1-R1 finds all mines except the M-14 while only picking up one piece of clutter at $(x = .60, y = -.50)$. The multistatic isofigure of this scenario misses two targets (M-14 mine and 5.08 cm diameter metal sphere) and has two false alarms; it also has a general loss of definition.

Placing the river rocks on the surface adds a significant amount of clutter to the problem. Figs. 13 and 14 show the migrated results using the same 2 layer model as in the clean surface scenario. Clearly, the larger,

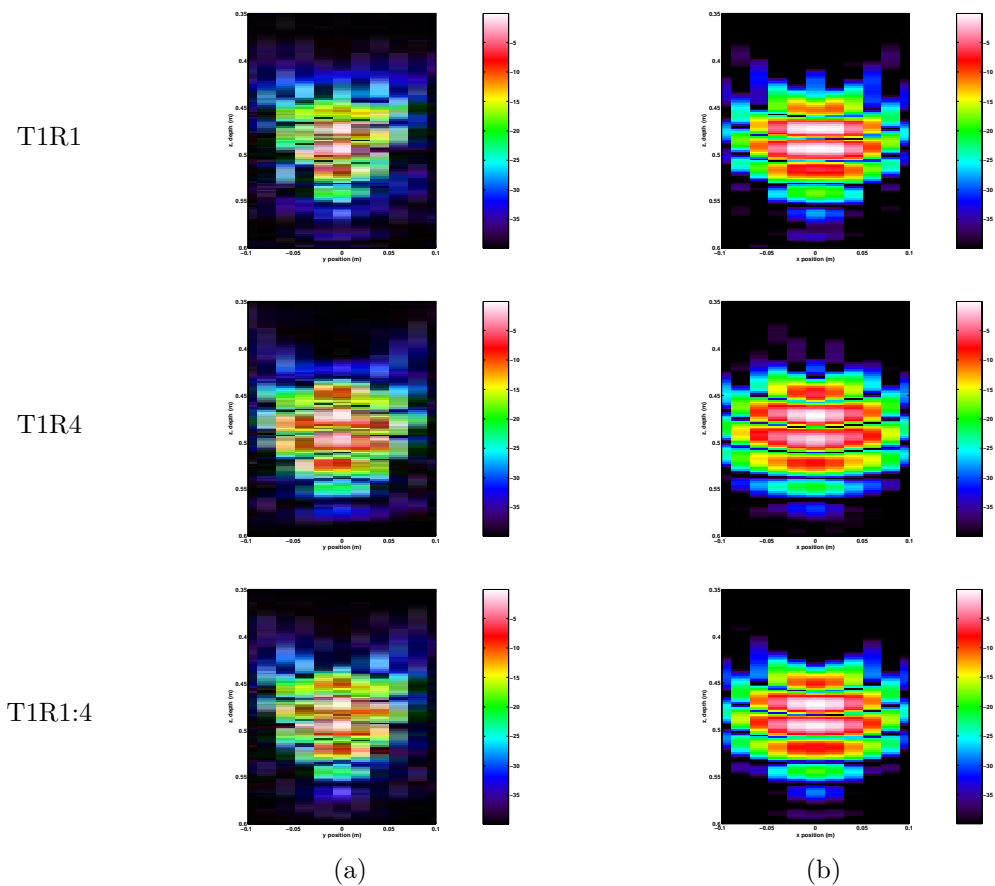


Figure 6. (a) Migrated slice of $x = 0$, (b) Migrated slice of $y = 0$.

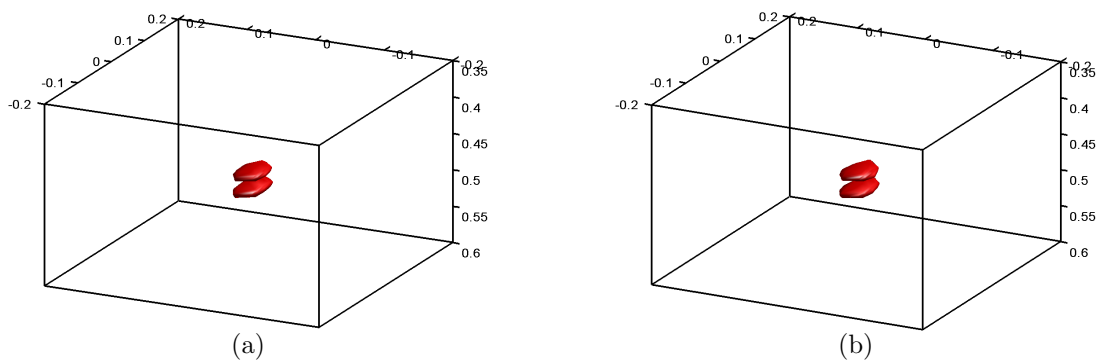


Figure 7. -5 dB Isofigure of migrated sphere with (a) T1-R1 only, (b) T1-R1:4.

deeper targets still show up well. Again, using coherent sums to combine the multistatic data appears to have no significant positive effect on the image quality. The arrows in Fig. 14 point out the image blobs formed by actual targets; the GPR does a surprisingly good job of finding targets in the dense clutter. In fact, for deep targets, the targets stand out clearly from the clutter.

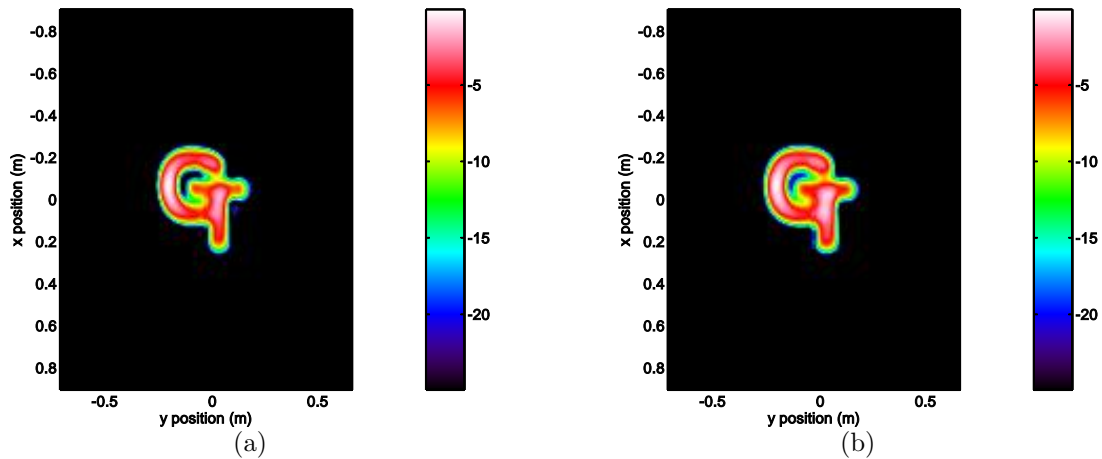


Figure 8. Slice of migrated GT sign with (a) T1-R1 only, (b) T1-R1:4.

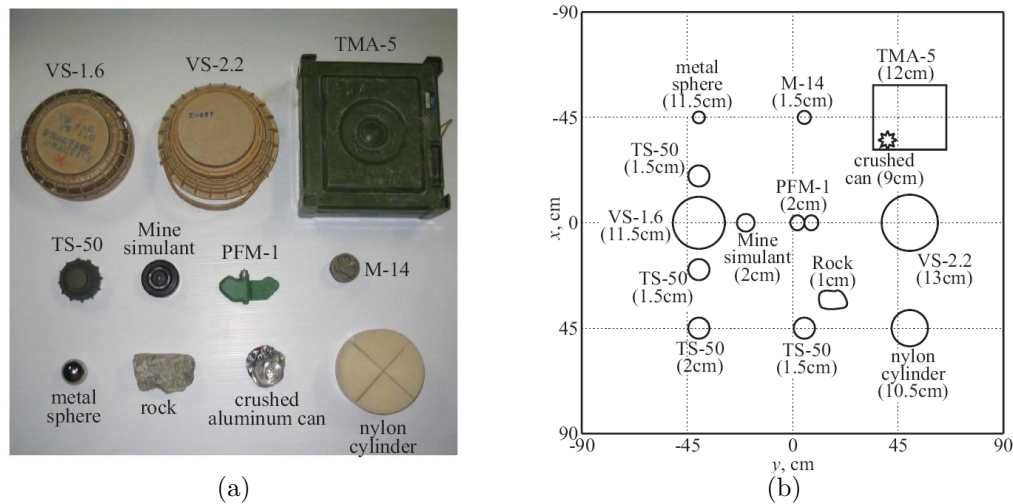


Figure 9. (a) Picture of Buried Targets, (b)Burial map of targets in sand. The numbers in the parentheses are the depths of the tops of the targets.

3.3. Buried Room

This experiment involves a chamber made of 2.54cm-thick Plexiglas. The exterior dimensions are $40.64 \times 30.48 \times 20.32$ cm. The chamber is buried at $(x = 0, y = 0)$ with the top 9.5cm from the ground. The surface of the sand is covered with river rocks. The data is processed with 1, 2 and 3 layer ground models to see the effect of the ground model. Figure 15 shows the energy sums of the migrated data for pair T1-R1 using different ground models.

To have a comparison between ground models, the the ratio of the energy within the chamber to the total energy of the migrated data is calculated. This ratio is found as 0.52, 0.4 and 0.46 for 1,2 and 3 layer models, respectively. This shows that because of the highly random reflection paths due to the rock layer, the 1 layer ground model performed better for imaging a deep target. When 4 multistatic pair images are combined by coherent addition the combined image shown in Fig 16 is obtained. The ratio of chamber area energy to the total energy for combined image is 0.71. This is a notable improvement over the best single pair result from any layer model.

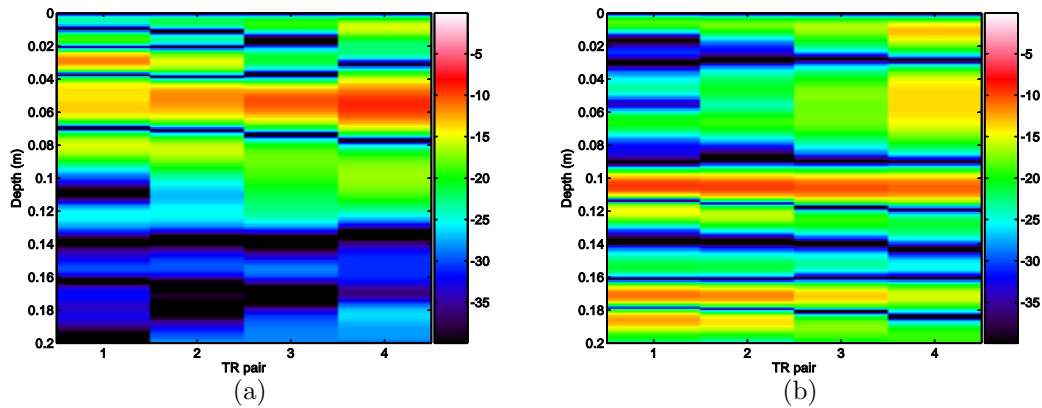


Figure 10. Moveout from narrowest 4 pairs of (a) shallow TS-50, (b) deep nylon cylinder.

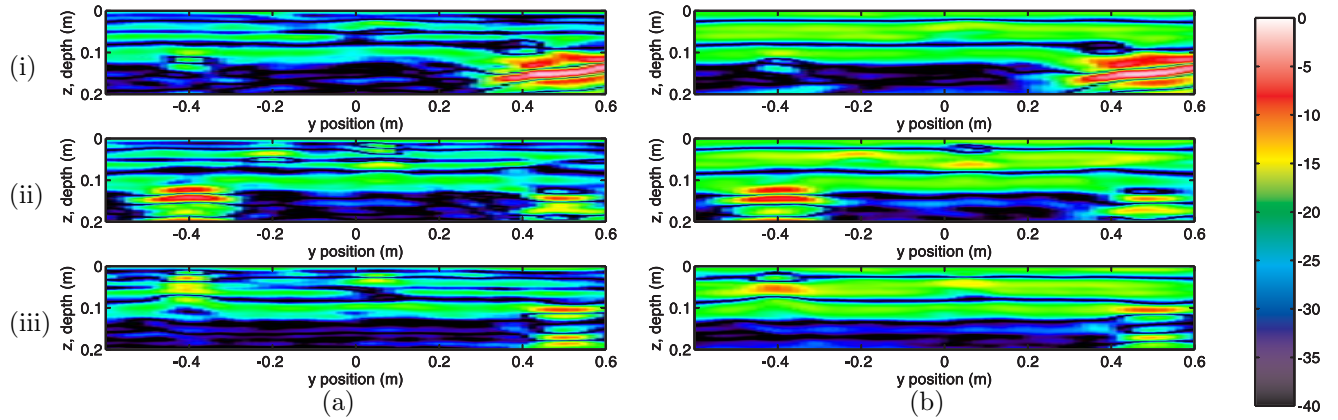


Figure 11. Migrated output slices at (i) $x = -45$, (ii) $x = 0$, (iii) $x = 45$ for (a) pair T1-R1, (b) coherent sum of T1-R1:4.

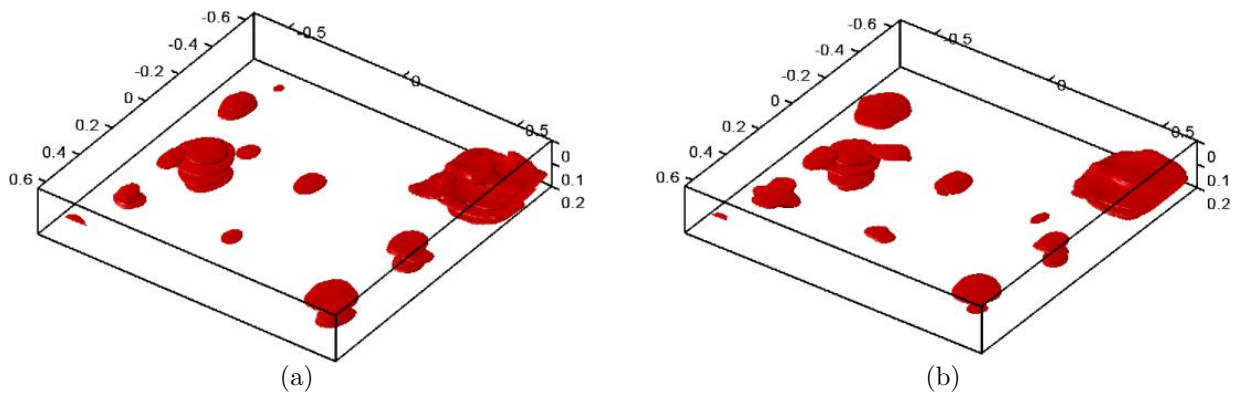


Figure 12. -16 dB isofigures of migrated data for (a) T1-R1 pair only, (b) Coherent combination of first 4 T-R pairs.

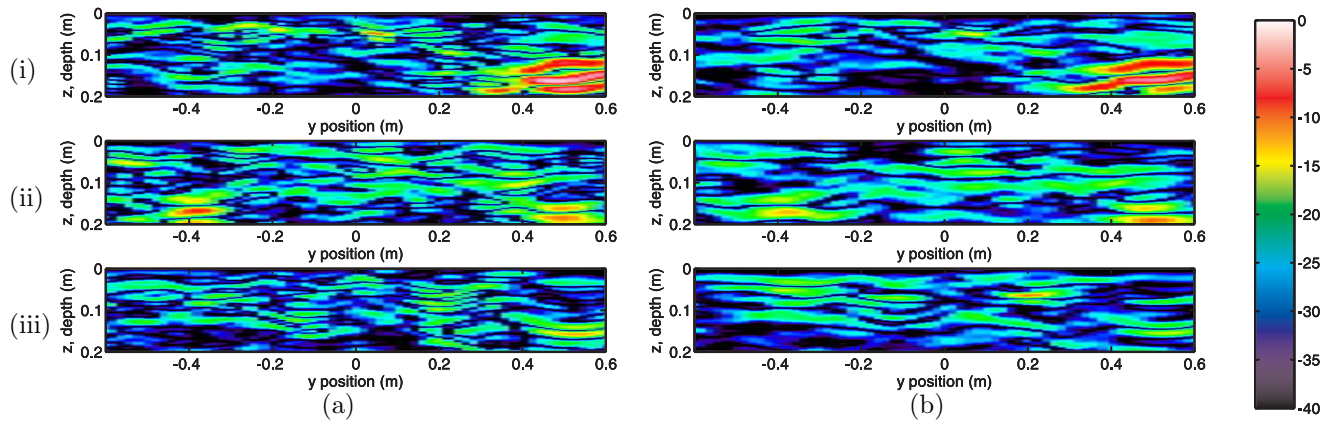


Figure 13. Migrated output slices of cluttered surface data at (i) $x = -45$, (ii) $x = 0$, (iii) $x = 45$ for (a) pair T1-R1, (b) coherent sum of T1-R1:4.

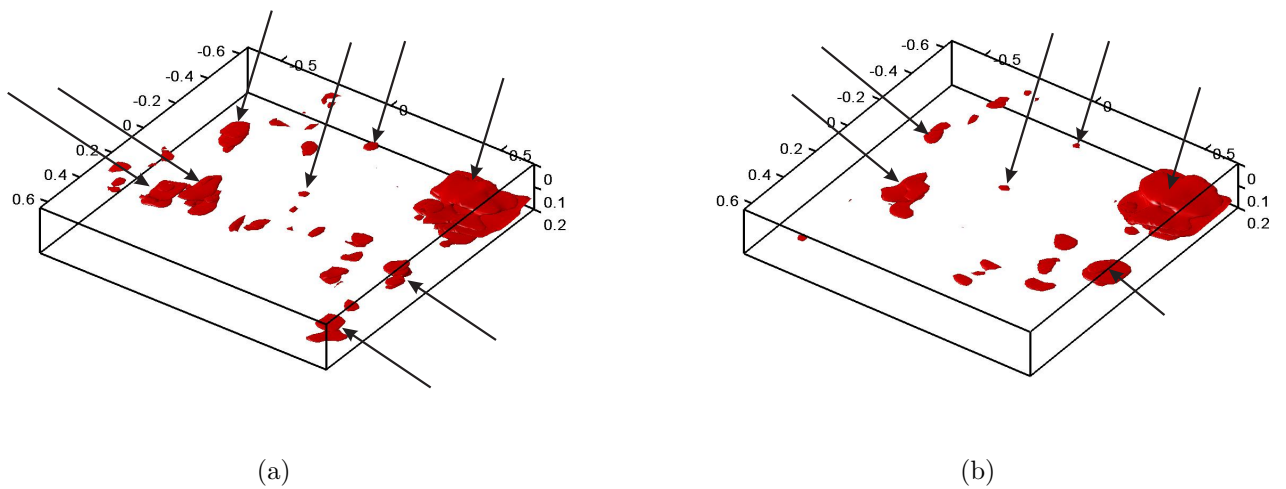


Figure 14. -15 dB isofigures of migrated cluttered surface data for (a) T1-R1 pair only, (b) Coherent combination of first 4 T-R pairs.

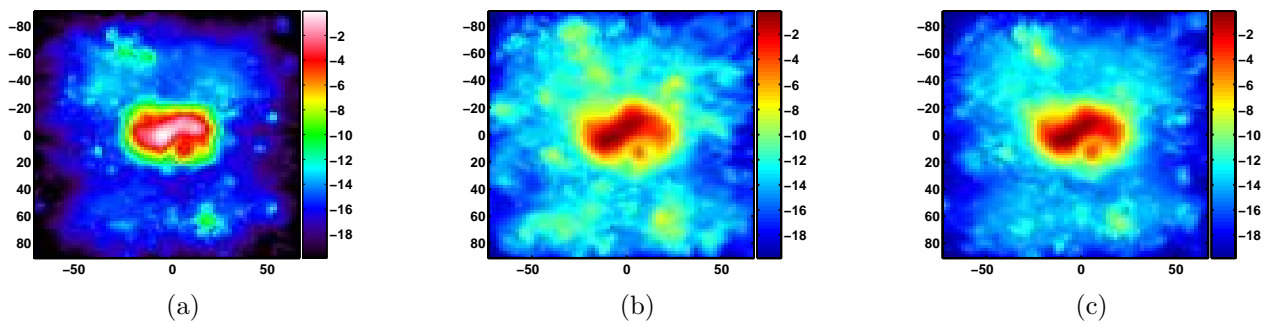


Figure 15. Backprojected images of pair T1-R1 using a (a) 1-layer, (b) 2-layer, (c) 3-layer model of the ground.

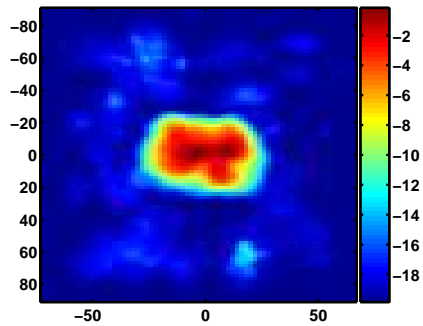


Figure 16. Energy summed to surface for coherent sum of pairs T1-R1:4 using 1 layer model.

4. CONCLUSIONS

The multistatic results in this paper only show a significant improvement for the deeply buried room. For the other cases, there was either non improvement or slight degradation of the image quality. In all of the cases there appears to be good time alignment between the pairs, and data such as that in Fig. 10 suggest that combinations of data should improve image quality. Using a coherent sum to combine the images is not sufficiently exploiting the potential of multistatic GPR imaging. This data does, however, bring to light certain possibilities for future improvements. The strong layering present in the clean surface mine migrations are most likely present even when the mines are not; if the time alignment is good enough, a scan over a known empty region would yield a bias signal that could be subtracted out of the data. Another possibility for boosting gains from multistatic pairs is to perform image detection on each T-R scan, and then combine the results of the detection outputs. Despite the fact that multistatic data is not yet improving image quality, there are still signs that it has not yet been fully exploited.

REFERENCES

1. D. J. Daniels, *Surface-penetrating radar*, London : Institution of Electrical Engineers, 1996.
2. K. Kim and W. S. Jr., "Design of a resistively-loaded vee dipole for ultra-wideband ground-penetrating radar applications," *IEEE Transactions on Antennas and Propagation* **53**, 2005.
3. K. Kim, A. C. Gurbuz, J. H. McClellan, and J. Waymond R. Scott, "A multi-static ground-penetrating radar with an array of resistively loaded vee dipole antennas for landmine detection," in *Detection and Remediation Technologies for Mines and Minelike Targets X, Proc. of SPIE*, **5794**, pp. 495–506, June 2005.
4. X. Feng and M. Sato, "Pre-stack migration applied to gpr for landmine detection," *Inverse Problems* **20**, pp. 99 – 115, 2004.
5. E. Johansson and J. Mast, "Three dimensional ground penetrating radar imaging using a synthetic aperture time-domain focusing," in *Proc. of SPIE Conference on Advanced Microwave and Millimeter Wave Detectors*, **2275**, pp. 205–214, 1994.